Accepted for publication in *The Astrophysical Journal*

Near-Infrared Spectroscopy of Molecular Hydrogen Emission in Four Reflection Nebulae: NGC 1333, NGC 2023, NGC 2068, and NGC 7023

Paul Martini, K. Sellgren, & D.L. DePoy

Department of Astronomy, 174 W. 18th Ave., Ohio State University,
Columbus, OH 43210
martini,sellgren,depoy@astronomy.ohio-state.edu

Abstract

This paper presents near-infrared spectroscopy of fluorescent molecular hydrogen (H_2) emission from NGC 1333, NGC 2023, NGC 2068, and NGC 7023 and derives the physical properties of the molecular material in these reflection nebulae. These observations of NGC 2023 and NGC 7023 and the physical parameters derived for these nebulae are in good agreement with previous studies. Both NGC 1333 and NGC 2068 have no previously-published analysis of near-infrared spectra. This study reveals that the rotational-vibrational states of molecular hydrogen in NGC 1333 are populated quite differently from NGC 2023 and NGC 7023. We determine that the relatively weak UV field illuminating NGC 1333 is the primary cause of the difference. Further, the density of the emitting material in NGC 1333 is of much lower density, with $n \sim 10^2 - 10^4$ cm^{-3}. NGC 2068 has molecular hydrogen line ratios more similar to those of NGC 7023 and NGC 2023. Model fits to this nebula show that the bright, H_2-emitting material may have a density as high as $n \sim 10^5$ cm^{-3}, similar to NGC 2023 and NGC 7023.

Our spectra of NGC 2023 and NGC 7023 show significant changes in both the near-infrared continuum and H_2 intensity along the slit and offsets between the peaks of the H_2 and continuum emission. These brightness changes may correspond to real changes in the density and temperatures of the emitting region, although uncertainties in the total column of emitting material along a given line of sight complicates the interpretation. The spatial difference in the peak of the H_2 and near-infrared continuum peaks in NGC 2023 and NGC 7023 shows that the near-infrared continuum is due to a material which can survive closer to the star than H_2 can.

Subject headings: infrared: spectra – interstellar: molecules – infrared: sources – nebulae: reflection – nebulae: individual (NGC 1333, NGC 2023, NGC 2068, NGC 7023)

1. Introduction

Molecular hydrogen (H_2) is the most abundant molecule in the universe. The study of this molecule has applications to a wide range of astrophysical questions ranging from the episode of reionization in the early universe to spectra of ultraluminous IR galaxies to star formation and photodissociation regions (PDRs) in our galaxy. In PDRs, including the reflection nebulae discussed in this paper, observations of H_2 line emission can be a valuable means of extracting physical information about the molecular material in areas of young star formation. Models of PDRs (see the recent review by Hollenbach & Tielens 1997) include predictions for the relative population of the rotational and vibrational levels of H_2 as a function of density, temperature, and the strength of the ultraviolet (UV) radiation field (Black & van Dishoeck 1987; Sternberg & Dalgarno 1989; Burton, Hollenbach, & Tielens 1990; Draine & Bertoldi 1996). As H_2 is a homonuclear molecule, it has no permanent dipole moment and therefore emits primarily via quadrupole transitions. The strongest of these transitions primarily occur in the near- and mid-infrared regions of the electromagnetic spectrum. The near-infrared $K-$band (centered at 2.2 μm), in particular, contains a number of well-separated emission lines and is relatively accessible from ground-based observatories.

Observations of molecular hydrogen line ratios have been used to estimate the physical properties of the reflection nebulae NGC 2023 (Gatley et al. 1987; Hasegawa et al. 1987; Takayanagi et al. 1987; Black & van Dishoeck 1987; Draine & Bertoldi 1996; Burton et al. 1998) and NGC 7023 (Martini, Sellgren, & Hora 1997). This information is valuable in conjunction with mid-infrared observations of the dust distribution and dust spectral features (Gatley et al. 1987; Cesarsky et al. 1996) for determining the nature and properties of the dust present in these regions. The study of nebulae with a range of densities and UV field strengths aids in understanding how physical conditions in nebulae affect the dust content, such as by investigating correlations between dust properties and the physical properties of the PDRs in which it is observed.

This paper presents near-infrared spectroscopy of molecular hydrogen line emission in four reflection nebulae: NGC 1333, NGC 2023, NGC 2068, and NGC 7023. The slit positions in these nebulae were chosen to coincide with mid-infrared spectroscopy of these regions with the *Infrared Space Observatory* (ISO). These observations include studies of two nebulae, NGC 1333 and NGC 2068, in which the H_2 emission spectrum has not been previously analyzed. For NGC 2023 and NGC 7023, we have observed new slit positions and compare these regions with physical parameters derived for other regions.

2. Observations and Data Reduction

The observations presented in this paper were obtained on observing runs in September-October 1997 (NGC 7023 and NGC 1333) and January-February 1998 (NGC 2023 and NGC 2068).

A log of our observations is presented as Table 1. These observations were obtained with the near-infrared imager/spectrometer OSIRIS (DePoy et al. 1994) on the 1.8m Perkins telescope at Lowell Observatory. We used the cross-dispersed mode for these observations, which includes a $4''.5 \times 60''$ slit oriented North-South. Slight vignetting by a loose piece of baffling decreased the effective slit length to $\sim 45''$. This mode has a 2-pixel resolution of $R = \lambda/\Delta\lambda = 565$ at 2.2 μm, 565 at 1.65 μm, and 535 at 1.25 μm. Figure 1 shows a model spectrum of H_2 line emission from Draine & Bertoldi (1996) smoothed to our resolution. This spectrum illustrates the rich spectrum of H_2 emission expected from a PDR and also how most of the lines in the $J-$ and $H-$bands are blended together in our data. The strongest lines and blends are marked in the figure and Table 2 lists the wavelengths and transitions of the lines that contribute to each of the blends.

We observed these targets in the standard ABBA pattern, where each on-source, 'B' observation consisted of a 60s exposure and each 'A', 60s sky exposure was obtained on a nearby, blank piece of sky. In addition to our target observations, we also observed several atmospheric standards each night within Δsec $z = 0.1$ of the airmass of our targets. After interpolating over the hydrogen lines in these stars, they were used to remove the wavelength-dependent atmospheric and system transmission. These stars were observed by offsetting the telescope north-south to move the star along the slit and using the mean, calculated with a sigma-rejection algorithm, of the observations to remove the night-sky lines. Dome flats, which were the difference of flats obtained with the dome lights on and with the lights off, were used to remove variations in the pixel-to-pixel sensitivity across the slit. The bright OH night sky lines (Oliva & Origlia 1992) were used to calculate the dispersion solution. A0V atmospheric standards were observed each night to place the counts in the $J-$, $H-$, and $K-$bands on a relative flux scale. We calculated the relative flux coefficients by fitting these stars with a 9600 K blackbody. This conversion varied little from night to night and we estimate the net uncertainty to be 5% in this conversion. We derived an absolute calibration for the 1-0 S(1) line intensity by placing synthesized apertures on our unpublished broadband and narrowband imaging data.

3. Data

3.1. NGC 1333

NGC 1333, also known as vdB 17 (van den Bergh 1966), is illuminated by BD +30 549 (Greenstein 1948; Racine 1968). Its spectral class is B8-9p based on photoelectric photometry (Johnson 1960), B8V based on a spectrum (Racine 1968), or B6 (Harvey, Wilking, & Joy 1984) based on its luminosity. Racine (1968) measured the extinction towards BD +30 549 to be $A_V = 1.86$ with $R_V = 3.1$. The distance to NGC 1333 is estimated to be 500 pc (Strom, Grasdalen, & Strom 1975). Our observed position in NGC 1333 is different from the better studied and more luminous NGC 1333/SVS-3 (e.g. Joblin et al. 1996; Bregman et al. 1993).

Sellgren (1986) first detected Q-branch H_2 emission near 2.4 μm from the reflection nebulosity in this region at a position 20″ south of BD +30 549 with a 12″ diameter beam. H_2 emission from the 1-0 S(1) and 2-1 S(1) lines was detected by Tanaka et al. (1989) at a position 40″ south of the central star with a beam diameter of 19.6″. Our long slit, oriented north-south and centered at 12″ east 26″ south of BD +30 549, overlaps the position observed by Tanaka et al. (1989).

Our spectrum of NGC 1333 includes detections of a number of lines in the near-infrared $K-$band, as well as a few of the more prominent, unblended lines in J and H. Before summing along the slit, we searched for any obvious structure in the H_2 line intensities. As suggested by our unpublished imaging data, no strong, filamentary structure was present in our slit and we therefore summed the full, useful (4.5″ × 45″) range to produce the spectrum shown in Figure 2. The relative line intensities, uncorrected for extinction, are listed in Table 3. Our narrowband imaging is not sensitive enough to directly measure the 1-0 S(1) line intensity. Instead, we measured the intensity of the continuum emission and used this to calibrate the strength of the 1-0 S(1) line from our spectrum to be $1 \pm 0.3 \times 10^{-5}$ erg s^{-1} cm^{-2} sr^{-1}.

3.2. NGC 2023

NGC 2023 is one of the brightest reflection nebulae in the sky and was the first source in which fluorescent H_2 emission was detected (Gatley et al. 1987; Sellgren 1986). This nebula, also known as vdB 52, is illuminated by the bright B1.5V star (Racine 1968) HD 37903. NGC 2023 is in the molecular cloud L1630 and is at a distance of $\sim$ 400 pc (Anthony-Twarog 1982). Racine (1968) estimated the extinction towards HD 37903 to be $A_V = 1.12$ with $R_V = 3.1$.

Gatley et al. (1987) mapped the nebula in the 1-0 S(1) line of H_2 and obtained low-resolution spectra at positions 80″ south and 160″ north of the HD 37903. These spectra showed a large number of features, including the 1-0 Q-branch in the $K-$band and the 6-4 and 5-3 Q-branches in the $H-$band. These spectra were also studied by Hasegawa et al. (1987) and Takayanagi et al. (1987). Sellgren (1986) detected Q-branch emission from positions 60″ and 80″ south of HD 37903. Additional H_2 lines have been observed in spectra obtained by Burton (1992) and described in more detail by Burton et al. (1998). Near-infrared images of the spatial distribution of H_2 through narrowband filters have been obtained by Field et al. (1994), Rouan et al. (1997), and Field et al. (1998).

We observed NGC 2023 at the position 60″ south of HD 37903 observed by Sellgren (1986). Our long slit also includes the region 80″ south observed by Gatley et al. (1987). This slit position is near, but to the east of the position observed by Burton et al. (1998). The Burton et al. position is centered on a peak in the H_2 emission located 78″ south, 9″ west of HD 37903 and was observed with a roughly 5″ diameter beam. Our spectrum extends from approximately 35″ to 84″ directly south of HD 37903.

The relative strength of the H_2 and continuum emission changes significantly along the length of our slit with the region from 35″ to 67″ south (hereafter the north region) showing strong continuum emission and weak H_2 lines. The region from 67″ to 84″ south (hereafter the south region), in contrast, shows negligible continuum emission but bright H_2 emission. Figure 3a shows the relative number of counts in the 1-0 S(1) line and the neighboring continuum as a function of position along the slit. Because of the significant differences in these two regions, we extracted them separately and show the north and south regions as Figures 4 and 5, respectively. The relative line intensities for both of these regions are listed in Table 3. As we do not have narrowband imaging data for NGC 2023, we used K' imaging data to measure the 1-0 S(1) line intensity by measuring the total flux in the K' band and then using our spectra to measure the fraction of the K' flux in the 1-0 S(1) line. The absolute 1-0 S(1) line intensity for the north region is $8 \pm 3 \times 10^{-5}$ erg s^{-1} cm^{-2} sr^{-1}, for the south region it is $1.2 \pm 0.4 \times 10^{-4}$ erg s^{-1} cm^{-2} sr^{-1}.

3.3. NGC 2068

NGC 2068, which is also known as vdB 59, is in the same molecular cloud (L1630) as NGC 2023 and is also estimated to be at a distance of approximately 400 pc (Anthony-Twarog 1982). Strom et al. (1975) classified the central star of this nebula, HD 38563-N as a B2III. Strom, Strom, & Vrba (1976) estimate the extinction towards HD 38563-N to be $A_V = 4$ based on $E(H-K)$. Recent imaging (Martini, DePoy, & Sellgren 1999) shows that HD 38563-N is actually a close ($\sim 2''$ separation) pair of stars with comparable JHK brightnesses. A low-resolution JHK spectrum ($R \sim 750$) of these stars obtained on 9 Sept 1998 shows that both stars are consistent with an early B-type classification based on the presence of weak hydrogen absorption features.

Sellgren (1986) unsuccessfully searched for H_2 emission from the Q-branch at a position 60″ east, 40″ south of HD 38563-N. Our unpublished narrowband images show no extended H_2 emission at this offset position. Based on these images we instead selected two positions, centered 72″ and 121″ east of HD 38563-N as the peaks of the continuum and H_2 emission, respectively. Throughout this paper these positions will be referred to as the "C-Peak" and the "H_2−Peak," respectively.

Only weak H_2 line emission was detected at the C-Peak 72″ east of HD 38563-N, even when the entire slit is averaged together. The spectrum of this region is shown in Figure 6. The bright line at 1.64 μm is probably [Fe II] $\lambda 1.644\mu$m. In principle, the strength of this line can be compared to the strength of other [Fe II] lines to derive densities or measure the extinction in the emitting region (e.g. Nussbaumer & Storey 1988). However, no other [Fe II] lines were detected in our spectrum and we can set no meaningful limits on the density or extinction at this slit position. As [Fe II] emission arises in partially or fully ionized gas in PDRs, the presence of [Fe II] and H_2 in this spectrum suggests the observation includes at least two different emitting regions along the line-of-sight, with ionized gas near the central star and H_2 emission from molecular material either in front of or behind the ionized gas.

The slit position centered on the H_2−Peak shows much stronger emission. Figure 7 is a sum of the slit over the 23″ region from 0″ to 23″ north, 121″ east of the central star. The relative line intensities corresponding to this region are listed in Table 3. The southern part of this slit position extends beyond the H_2 emission filament into a region containing no strong H_2 or continuum emission. For the H_2−Peak, the 1-0 S(1) line intensity is $3.1 \pm 0.8 \times 10^{-5}$ erg s^{-1} cm^{-2} sr^{-1}. 1-0 S(1) line emission was not clearly detected at the continuum region in our narrowband data. Instead, we used the intensity of the continuum region to calibrate the 1-0 S(1) line in our spectrum, as we did for NGC 1333. The 1-0 S(1) line intensity is $7 \pm 3 \times 10^{-6}$ erg s^{-1} cm^{-2} sr^{-1}.

3.4. NGC 7023

NGC 7023, also known as vdB 139, is a bright reflection nebula illuminated by the pre-main-sequence B3e star HD 200775 (Johnson 1960; Racine 1968; Witt & Cottrell 1980). The distance to NGC 7023 is estimated to be 440 pc (Whitcomb et al. 1981). We adopt a visual extinction of $A_V = 2.2$ with $R_V = 5$ as discussed by Martini et al. (1997). Observation of the H_2 Q-branch emission from NGC 7023 was first attempted, though unsuccessfully, by Sellgren (1986) at a position 30″ west and 20″ north of HD 200775. Narrowband imaging in the 1-0 S(1) and 2-1 S(1) lines (Lemaire et al. 1996) later revealed the presence of fluorescently excited H_2 in the bright filaments seen in this nebula at 2.1 μm by Sellgren, Werner, & Dinerstein (1992). Near-infrared spectroscopy of two of these filaments by Martini et al. (1997) showed that the bulk of this emission was due to UV fluorescence in filaments with densities of $10^4 - 10^6$ cm^{-3}.

Our observations are centered on a position 27″ west, 34″ north of HD 200775. This position is close to, but not overlapping, the slit position "P1" (40″ west, 34″ north) of Martini et al. (1997). As in the case of NGC 2023, the spectrum of NGC 7023 shows significant changes in both continuum and H_2 line intensity across the slit. The slit is centered on a bright filament, where the total (H_2+continuum) emission is brightest (hereafter the H_2−peak region, $32 - 41''$ north). The spectrum of this region is shown in Figure 8. The H_2 and continuum emission have noticeably different behavior on either side of this peak. The H_2 emission lines are still fairly strong in the region $41 - 56''$ north (hereafter the north region; see Figure 9) of the filament, while they are significantly weaker in the region $12 - 32''$ to the south (hereafter the south region; not shown) of the filament, closer to HD 200775. The relative line intensities for the peak and north regions are listed in Table 3. In contrast, the continuum emission is brightest in the south region, somewhat less bright at the H_2−peak, and quite weak in the north region. The behavior of the 1-0 S(1) line and the neighboring continuum are shown in Figure 3b. For the H_2−Peak, the 1-0 S(1) line absolute intensity is $6.8 \pm 1.7 \times 10^{-5}$ erg s^{-1} cm^{-2} sr^{-1}. For the north region, the 1-0 S(1) line intensity is $4 \pm 1 \times 10^{-5}$ erg s^{-1} cm^{-2} sr^{-1}. Our improved narrowband calibration results in significantly lower line intensities for the positions "P1" and "P2" reported by Martini et al. (1997). For these positions the intensities are $8 \pm 2 \times 10^{-5}$ erg s^{-1} cm^{-2} sr^{-1} and $4.6 \pm 1.2 \times 10^{-5}$ erg s^{-1} cm^{-2} sr^{-1}, respectively; this new flux calibration does not change any of the conclusions of Martini et al. (1997).

4. Results

In order to derive information about the densities, temperatures, and incident UV fields in these PDRs, we compared the relative level populations of the rotational-vibrational levels of H_2 derived from these spectra with the model predictions of Draine & Bertoldi (1996). As these models are all characterized by UV-field-to-density ratios (G_0/n_H) of 0.1 or 0.01, our best-fitting density models are reported for $G_0/n_H = 0.1$ or $G_0/n_H = 0.01$ (Draine & Bertoldi 1996 denote the UV field strength as χ). G_0 is a unit of measure of the UV field strength in units of the average interstellar radiation field at $\lambda = 1000$ Å as defined by Habing (1968). A value of $G_0 = 1$ implies a UV field strength of 4×10^{-14} erg cm^{-3} (see also Draine & Bertoldi 1996). The modeling procedure is described in detail by Martini et al. (1997), although we have modified the technique somewhat for this work. Briefly, we compared our observations with these models by using the χ^2 parameter as a measure of the goodness of fit between each model and the data. All of the lines with relatively good ($> 2\sigma$) detections from a given slit position were used in the fitting procedure, except for the 2-1 S(4) line, as it lies on a strong telluric absorption feature, and the 1-0 S(3) line, as it lies in a region where the atmospheric+filter transmission has very steep gradient.

Before performing these model fits, we corrected the observed relative line intensities for the effects of interstellar extinction. We used the values for the stellar extinction and reddening laws quoted above to deredden our measured line intensities following the procedure described by Mathis (1990). However, the nebular extinction may be higher or lower than the stellar extinction. Martini et al. (1997) found that varying the assumed A_V towards NGC 7023 by a factor of 2 had no significant effect on their results. We tested the sensitivity of all of the fits to the assumed value of A_V by also running fits with $\Delta A_V = \pm 1$; reddening variations of this magnitude do not affect our results. Ideally, the extinction towards these regions should be computed by measuring the line strengths of two lines arising from the same upper level and thus whose ratios are determined only by their relative transition probabilities and statistical weights. Unfortunately we did not detect such a pair of lines in any of our objects. However, extinction is not a severe problem for our modeling procedure as most of the features lie in the $K-$band and so are both close together in wavelength and relatively insensitive to the extinction.

The main differences between the current work and the technique described by Martini et al. (1997) are that we performed the χ^2 fit on the line intensity data, rather than on the relative column density in each level population, and that we included the intensities of several blends of lines in our fitting procedure. Figure 10a shows the variation of one of these blends, H4, as a function of density, UV field strength, and temperature. The intensity of this blend relative to the 1-0 S(1) line is sensitive to density, though increasing the UV field strength or the gas temperature tends to mimic the effect of increasing density. The behavior of this blend is representative of the other blends listed in Table 2 because all of these blends are dominated by transitions from high vibrational levels. Their intensity relative to the 1-0 S(1) transition decreases with increasing density as the population of the $v = 1$ level is increased by collisions.

Wolniewicz, Simbotin, & Dalgarno (1998) have recently recalculated the spontaneous electronic quadrupole transition probabilities for H_2. While these values are a significant improvement over the work of Turner, Kirby-Docken, & Dalgarno (1977) for transitions with probabilities of 10^{-9} or less, their values for the higher probability transitions, which include the lines in our spectra, are not appreciably different.

In addition to the model fits of all of the detected lines and blends with the models, we also examined the ratios of several select lines that have been used in the past as diagnostics of PDRs. These lines include the ratio of the 1-0 S(1) line to the 2-1 S(1) line and the ratio of the 2-1 S(1) line to the 6-4 Q(1) line. The 1-0 S(1)/2-1 S(1) line ratio is a good diagnostic of the density because the rate of collisional deexcitation of the $v = 2$ level increases faster than that of the $v = 1$ level. Thus this ratio increases substantially when the density is near the critical density of H_2, $n_{crit} = 10^5$ cm^{-3}. The 2-1 S(1)/6-4 Q(1) line ratio compliments the 1-0 S(1)/2-1 S(1) line ratio as it is much less sensitive to collisional deexcitation. Draine & Bertoldi (1996) show the behavior of these two line ratios as a function of density, UV field strength, and gas temperature for their models (see their Figures 15 and 16). However, that the 2-1 S(1)/6-4 Q(1) line ratio is fairly sensitive to reddening compared to the 1-0 S(1)/2-1 S(1) ratio. For example, adding $A_V = 5$ magnitudes of reddening with an $R_V = 3.1$ reddening law (e.g. Mathis 1990) will decrease the 1-0 S(1)/2-1 S(1) ratio by 5%, but increase the 2-1 S(1)/6-4 Q(1) ratio by 30%.

Figure 10b shows the ratio of the 1-0 S(7) line to the intensity of the H4 blend discussed above. As these two features are very close in wavelength, their ratio is very insensitive to extinction and the reddening law. An error of $A_V = 5$ magnitudes will only increase this ratio by $\sim 1\%$. As in the case of the ratio of the H4 blend to the 1-0 S(1) line, this ratio combines the H4 intensity, dominated by transitions from high vibrational levels, with a transition from the $v = 1$ level, which is sensitive to increasing density, particularly as the density approaches n_{crit}. At low densities ($n < 10^4$cm^{-3}) when this ratio is small, this diagnostic is fairly insensitive to variations in UV field strength and gas temperature. At higher densities, however, increasing UV field strength and temperature mimic the effect of a higher density.

Other diagnostics of the physical conditions in PDRs include the rotational temperature (T_{rot}), vibrational temperature (T_{vib}), and the ratio of ortho$-$ to para$-H_2$ (γ). The rotational (or vibrational) temperature is measured from the slope of a line passing through data with the same vibrational (or rotational) upper levels on diagrams of the [ln(N_u/g_u), T_u]$-$plane, where N_u, g_u, and T_u are, respectively, the column density, statistical weight, and energy (in Kelvin) of the upper level. Population diagrams derived from our spectra showing the distribution of ln(N_u/g_u) vs. T_u are shown in Figures 11 and 12. Differences between T_{rot} and T_{vib} are an indicator of fluorescently excited H_2, while purely thermally excited H_2 results in equal T_{rot} and T_{vib} (Black & Dalgarno 1976; Black & van Dishoeck 1987; Takayanagi, Sakimoto, & Onda 1987; Tanaka et al. 1989; Draine & Bertoldi 1996). In this paper T_{rot} was measured by fitting a line to [ln(N_u/g_u, T_u] for the 1-0 S(0) and 1-0 S(2) lines; we chose this pair of lines because they are both bright and are even rotational states, which avoids uncertainty in γ. T_{vib} was measured with the 1-0 S(1) and

2-1 S(1) lines.

H_2 is assumed to form on grain surfaces with $\gamma = 3$ (e.g. Spitzer & Zweibel 1974), but after formation this ratio can change with time (Dalgarno, Black, & Weisheit 1973; Flower & Watt 1984; Tielens & Allamandola 1987; Hasegawa et al. 1987; Tanaka et al. 1989; Burton et al. 1992; Chrysostomou et al. 1993; Draine & Bertoldi 1996). In these nebulae, γ was measured with the $v = 1$, $J = 2 - 4$ levels. Draine & Bertoldi (1996) predict $\gamma = 2 \pm 0.2$ for $v = 1, J = 2 - 7$ in their model PDRs and show that γ only weakly depends on density and UV field strength. Sternberg & Neufeld (1999) explain how optical depth effects in the UV Lyman and Werner bands result in a lower observed γ for the excited H_2 than the $\gamma = 3$ predicted by theory for gas above 200 K.

4.1. NGC 1333

Model fits to NGC 1333 show that it is best fit by models with $n = 10^2 - 10^3$ cm^{-3} for $G_0/n_H = 0.1$ and $n = 10^4$ cm^{-3} for $G_0/n_H = 0.01$. NGC 1333 is illuminated by a B8V star and the UV field is expected to be $G_0 = 140$ (Uchida et al. 1999). The results of comparing these spectra with model predictions is thus in reasonable agreement with the expected UV field. Warin et al. (1996) derive densities of 3×10^3 to 5×10^4 cm^{-3} in the central regions of NGC 1333 based on CO observations, which also agree with our results, as does our estimate of the intensity of the 1-0 S(1) line.

The results of using individual line ratios support our model results. The 1-0 S(1)/2-1 S(1), 2-1 S(1)/6-4 Q(1), and 1-0 S(7)/H4 ratios (see Table 6) all predict densities of $\sim 10^4$ cm^{-3}. The 2-1 S(1)/6-4 Q(1) line ratio allows densities of up to 10^5 cm^{-3}, but this line ratio is also the most sensitive to extinction. The extinction estimate towards NGC 1333, and for all of the nebulae discussed here, is based on a line-of-sight estimate to the central star. Any additional dust screen towards the excited molecular gas would increase the extinction and in turn lead to a smaller observed 6-4 Q(1) intensity and drive the observed 2-1 S(1)/6-4 Q(1) ratio to a higher value. However, as mentioned above, variations in $\Delta A_V = \pm 1$ neither changed the best-fitting model parameters nor the quality of the fit.

Our measurements of T_{rot} and T_{vib} shows that T_{vib} is significantly higher than T_{rot}, a further indicator that the H_2 emission in NGC 1333 is fluorescent, and $\gamma = 1.4 \pm 0.4$. Such a low value is in agreement with the low density, UV field, and temperature derived above. However, as mentioned above, Draine & Bertoldi (1996) found in their model PDRs that γ is not a strong constraint on density and UV field strength.

4.2. NGC 2023

The density of NGC 2023 has been previously estimated to be approximately 10^5 cm^{-3} with $G_0 \sim 5000$ using a variety of techniques (Burton et al. 1990; Fuente et al. 1995; Draine & Bertoldi 1996; Wyrowski et al. 1997; Field et al. 1998). Our analysis of the continuum-bright, or north region, yields a best-fit density of $n = 10^4 - 10^5$ cm^{-3} for $G_0/n_H = 0.1$ and $n = 10^5 - 10^6$ cm^{-3} for $G_0/n_H = 0.01$. For the H_2 bright, or south region, the best-fitting models predict a density of $n = 10^5$ cm^{-3} for $G_0/n_H = 0.1$ and $n = 10^6$ cm^{-3} for $G_0/n_H = 0.01$. These values are also in agreement with our measurements of the 1-0 S(1) line intensities at these two slit positions.

The relative line ratios of both the north and south regions agree well with a $n = 10^5$ cm^{-3} model and each other, which is consistent with our more extensive model fitting. This also suggests that the overall intensity difference (Figure 3) between the H_2−bright and continuum-bright regions do not mark a significant change in the physical properties of the PDR.

Our measurements of T$_{rot}$ and T$_{vib}$ at both positions in NGC 2023 are in good agreement with the measurements of Hasegawa et al. (1987). These results are also consistent with the density and temperature ranges discussed above as well as the particular models developed by Draine & Bertoldi (1996) for NGC 2023. Our derived value of $\gamma \sim 2$ is also consistent with the ortho-to-para ratio found by Hasegawa et al. (1987) and the model fit of Draine & Bertoldi (1996).

4.3. NGC 2068

We modeled both the continuum region and H_2−bright filament observed in NGC 2068. The continuum region had significantly fainter line emission than the H_2 filament and the models do not strongly constrain the physical conditions from this region. The best-fit models for the continuum region constrain the density to be $n = 10^2 - 10^4$ cm^{-3} for $G_0/n_H = 0.1$ and $n = 10^2 - 10^5$ cm^{-3} for $G_0/n_H = 0.01$. As discussed previously, the weak H_2 observed towards this region could be from relatively lower density material along the line of sight, but farther from the central star. In the H_2−bright region the density is constrained to be in the range $n = 10^3 - 10^5$ cm^{-3} for $G_0/n_H = 0.1$ and $n = 10^5 - 10^6$ cm^{-3} for $G_0/n_H = 0.01$. Our measurement of the line intensity of the 1-0 S(1) line suggests $n = 10^4$ cm^{-3} for $G_0/n_H = 0.1$ and $n = 10^5$ cm^{-3} for $G_0/n_H = 0.01$, which is also in agreement with the CS observations of Lada, Evans, & Falgarone (1997). Uchida et al. (1999) estimate $G_0 = 520$ at an angular distance of $93''$ from HD 38563-N, corresponding to $G_0 = 870$ at the projected distance of the continuum region and $G_0 = 310$ at the projected distance of the H_2−bright filament. The values are consistent with all but the highest density model fits. The 1-0 S(1) line intensity for the continuum region suggests the density is $n = 10^3 - 10^4$ cm^{-3}.

We only detected enough lines to measure the 1-0 S(1)/2-1 S(1) ratio in the continuum region. This ratio is consistent with a low density $n \leq 10^4$ cm^{-3} PDR with $T < 1000$ K. At the H_2 peak all three ratios and these values imply a density of $n \sim 10^4$ cm^{-3}. Measurements of T$_{rot}$, T$_{vib}$, and

γ are listed in Table 6 and are consistent with the model fits described above. Unfortunately, the H_2−Peak in NGC 2068 is located due west of the central star and this nebula was observed with a slit oriented north-south. We are thus not able to examine changes in the PDR as a detailed function of distance from the central star (and presumably as a function of UV field strength) as in NGC 2023 and NGC 7023.

4.4. NGC 7023

We carried out model fits to all three regions in the slit at the position NGC 7023 ISO-1 described in section 3. In the southern region, closest to HD 200755, the 1-0 S(0) and 1-0 S(1) lines were only weakly detected and thus we could not set useful limits on the physical parameters. At the position of the H_2 peak, and in the region north of the filament, we detected a number of lines. Model fits to the H_2−peak constrain the density to be $n = 10^6$ cm^{-3} for $G_0/n_H = 0.1$ and 0.01. Draine & Bertoldi's model fit to NGC 2023 (n2023b) with $n = 10^5$ cm^{-3} for $G_0/n_H = 0.05$ was also a good fit to this region. The 1-0 S(1) line intensity is also roughly consistent with these physical parameters. For the north region, our model fits yield $n = 10^5$ cm^{-3} for $G_0/n_H = 0.1$ and $n = 10^5 - 10^6$ cm^{-3} for $G_0/n_H = 0.01$. The models with $n = 10^5$ cm^{-3} for $G_0/n_H = 0.05$ were also a good fit to this region. The results for both of these regions agree with the density range and G_0 values ($n = 10^5 - 10^6$ cm^{-3}, $G_0 = 10^3 - 10^4$) found by Martini et al. (1997), the value of $G_0 = 2.6 \times 10^3$ found by Chokshi et al. (1988), and our line intensity measurement. The H_2−peak is at a projected distance of 0.1 pc from HD 200775, and so our results are also in agreement with the estimate that $G_0 = 300 - 1200$ at a distance of $0.1 - 0.2$ pc from HD 200775 by Federman et al. (1997).

The spectrum of NGC 7023 ISO-2 (not shown) showed only very weak emission from the 1-0 S(1) line. We therefore did not have enough information to model the molecular hydrogen emission at this slit position. The strength of this emission, relative to that detected at NGC 7023 ISO-1 in a similar integration time, implies that the density or total column density of H_2−emitting material is less in this region. Also, given its greater distance from the central star, in projection, this region is probably exposed to a lower UV radiation field.

The measured 1-0 S(1)/2-1 S(1) line ratios at the H_2−Peak and in the north region were 3.53 and 2.70, respectively. These two ratios are in broad agreement with the model fits described above. While the value at the H_2−Peak does imply a higher density than in the north region, an increase in this ratio could also be due to changes in the gas temperature and UV field strength. Both of these quantities could vary as the north region is farther, in projection, from the central star. The value of the 1-0 S(7)/H4 ratio similarly decreases from the H_2−Peak to the north region, though changes in this ratio with density are also degenerate with changes in temperature and UV field strength at densities approaching the critical density.

Our measurements of T_{rot} and T_{vib} at the H_2−Peak are in reasonable agreement with the measurement of Martini et al. (1997) at a different position on the same filament. These results are higher than those found by Lemaire et al. (1996), but are within their uncertainties. The measured $T_{rot} = 860 \pm 230$ is also in agreement with the predictions of the best model fits to this position discussed above. The value of γ is also consistent with both the observations of Martini et al. (1997) and the models.

5. Continuum and H_2 Emission

There are several models for the origin of the near-infrared continuum in reflection nebulae. One model suggests that the near-infrared continuum is due to thermal emission from tiny grains which are briefly heated by the absorption of single UV photons (Sellgren, Werner, & Dinerstein 1983; Sellgren 1984). Other models suggest a quasi-continuum of overlapping bands from polycyclic aromatic hydrocarbon (PAH) molecules (Léger & Puget 1984; Allamandola, Tielens, & Barker 1985), electronic fluorescence in PAHs (Allamandola, Tielens, & Barker 1989), or luminescence from hydrogenated amorphous carbon grains (Duley & Williams 1988; Duley 1988).

This continuum is not due to scattered starlight. Sellgren, Werner, & Allamandola (1996), in a survey of 23 reflection nebulae, found that all of these objects have similar near-infrared colors, independent of the spectral type of the central star. Sellgren, Werner, & Dinerstein (1992) observed NGC 2023 and NGC 7023 in polarized light and calculated that less than 20% of the 2.2 μm continuum emission, in contrast to the visible continuum, is due to scattered starlight. For NGC 7023, the small contribution of scattered light at K ($4 - 5\%$ polarization) compared to the larger scattered light contribution at J ($20 - 25\%$ polarization) is confirmed by our spectra (Figures 8 & 9), which show Paβ emission at 1.28 μm scattered from the central Be star, but no Brγ emission scattered from the Be star at 2.17 μm.

Our high signal-to-noise ratio, long-slit spectral observations of NGC 2023 and NGC 7023 are able to directly investigate the relative intensity of the 2.2 μm continuum and 1–0 S(1) line as shown in Figure 3. These observations show that the 2.2 μm continuum peaks closer to the central star than the H_2 emission in both NGC 2023 and NGC 7023. Our results at high spectral resolution confirm previous results from narrowband and broadband imaging of the near-infrared continuum and H_2 in NGC 2023 (Gatley et al. 1987; Field et al. 1994) and NGC 7023 (Lemaire et al. 1996). These images suggest that the near-infrared continuum peaks closer to the central star than does the fluorescent H_2 emission and that the near-infrared continuum emission is less filamentary than the H_2 emission.

The 3.3 μm emission feature, like the near-infrared continuum, has been proposed to arise from aromatic molecules or from aromatic grains, emitting either by fluorescence or by thermal emission during temperature fluctuations (see reviews by Puget & Léger 1989; Allamandola et al. 1989; Sellgren 1994; Papoular et al. 1996). The observational relationship between the near-infrared continuum and the 3.3 μm feature, however, is unclear. The near-infrared continuum and the 3.3 μm feature are always observed together in spectra of reflection nebula (Sellgren, Werner, & Dinerstein 1983; Sellgren, Werner, & Allamandola 1996). Sellgren, Werner, & Allamandola (1996) find that the ratio of the 3.3 μm feature to the nearby continuum is independent of the spectral type of the central star, but they also find approximately a factor of 3 variation in the feature-to-continuum ratio. This variation in the feature-to-continuum ratio is found both within an individual source and among different sources. Gatley et al. (1987) conclude from broadband imaging data that the near-infrared continuum in NGC 2023 is concentrated closer to the central star than is the 3.3 μm feature. These observations suggest that while the materials and emission mechanisms giving rise to the near-infrared continuum and 3.3 μm emission feature may be similar, they are not identical.

Observations of the 3.3 μm emission feature in NGC 2023, NGC 1333/SVS-3, and Parsamyan 18 show that the 3.3 μm feature is cospatial, in projection, with the H_2 emission in these three reflection nebulae (Gatley et al. 1987; Burton et al. 1989). This is in contrast to results from regions with stronger UV fields, such as the Orion Nebula (Burton et al. 1989; Sellgren et al. 1990; Tielens et al. 1993) and the planetary nebula NGC 7027 (Graham et al. 1993), where the 3.3 μm emission peaks closer to the UV source than the H_2 emission. In regions with stronger UV fields, the near-infrared continuum due to tiny grains or large molecules is swamped by free-free emission from ionized hydrogen. The absence of significant free-free emission in NGC 2023 and NGC 7023, however, allows a direct comparison of the location of the near-infrared continuum and H_2 emission. In these two reflection nebulae the 2 μm continuum peaks closer to the star than the H_2 emission. Thus it appears that in reflection nebulae the material responsible for the near-infrared continuum is able to survive closer to the central star than the molecular gas. This places an interesting constraint on laboratory analogs and theoretical models for the continuum emission.

6. Conclusions

We have obtained near-infrared spectroscopy of four reflection nebulae, including NGC 1333 and NGC 2068 for which no previous near-infrared spectra have been analyzed. We have used these spectra to determine the physical environments of these four nebulae and derived their physical properties by fitting the models of Draine & Bertoldi (1996) to the observed line ratios. The three brightest nebulae in our sample, NGC 2023, NGC 2068, and NGC 7023, all show significant structure on scales of $\sim 2''$, corresponding to physical sizes of $\sim$ 1000 AU at the distances of the nebulae. This structure corresponds to changes in density, continuum radiation, and the strength of the incident UV field, and serves as direct evidence of the very inhomogeneous or clumpy nature of these PDRs. In addition to variations in the H_2 emission, we have spectroscopy of the underlying near-infrared continuum in NGC 2023 and NGC 7023 with sufficient signal-to-noise ratio to trace the peaks in surface brightness of the H_2 1-0 S(1) line relative to the continuum along our long slit. This analysis shows that the near-infrared continuum, particularly at 2.2 μm where scattered starlight is negligible, peaks closer to the central star than the H_2 emission in both nebulae. This result shows that the material responsible for the near-infrared continuum can survive closer to the central star than the molecular hydrogen gas.

This work was supported in part by NASA grant NAG 5-3366 to KS. We would like to thank the staff of Lowell Observatory for their support during these observing runs and Rick Pogge for many helpful discussions.

REFERENCES

Allamandola, L. J., Tielens, A. G. G. M., & Barker, J. R. 1985, ApJ, 290, L25

Allamandola, L. J., Tielens, A. G. G. M., & Barker, J. R. 1989, ApJS, 71, 733

Anthony-Twarog, B. J. 1982, AJ, 87, 1213

Bregman, J., Rank, D., Sandford, S. A., & Temi, P. 1993, ApJ, 410, 668

Black, J. H. & Dalgarno, A. 1976, ApJ, 203, 132

Black, J. H. & van Dishoeck, E. F. 1987, ApJ, 322, 412

Burton, M. G., Hollenbach, D. J., & Tielens, A. G. G. M. 1990, ApJ, 365, 620

Burton, M. G., Howe, J. E., Geballe, T. R., & Brand, P. W. J. L. 1998, PASA, 15, 194

Cesarsky, D., Lequeux, J., Abergel, A., Perault, M., Palazzi, E., Madden, S., & Tran, D. 1996, A&A, 315, L305

Chokshi, A., Tielens, A. G. G. M., Werner, M. W., & Castelaz, M. W. 1988, ApJ, 334, 803

Chrysostomou, A., Brand, P. W. J. L., Burton, M. G., & Moorhouse, A. 1993, MNRAS, 265, 329

Dalgarno, A., Black, J. H., & Weisheit, J. C. 1973, Astrophys. Lett., 14, 77

Draine, B. T. & Bertoldi, F. 1996, ApJ, 468, 269

Duley, W. W. & Williams, D. A. 1988, MNRAS, 230, 1

Duley, W. W. 1988, MNRAS, 234, 61

Federman, S. R., Knauth, D. C., Lambert, D. L., & Andersson, B-G 1997, ApJ, 489, 758

Field, D., Gerin, M., Leach, S., Lemaire, J. L., Pineau des Forêts, G., Rostas, F., Rouan, D., & Simons, D. 1994, A&A, 286, 909

Field, D., Lemaire, J. L., Pineau des Forêts, G., Gerin, M., Leach, S., Rostas, F., & Rouan, D. 1998, A&A, 333, 280

Fuente, A., Martin-Pintado, J., & Gaume, R. 1995, ApJ, 442, L33

Gatley, I., Hasegawa, T., Suzuki, H., Garden, R., Brand, P., Lightfoot, J., Glencross, W., Okuda, H., & Nagata, T. 1987, ApJ, 318, L73

Graham, J. R., Serabyn, E., Herbst, T. M., Matthews, K., Neugebauer, G., Soifer, B. T., Wilson, T. D., & Beckwith, S. 1993, AJ, 105, 250

Greenstein, J. L. 1948, ApJ, 107, 375

Harvey, P. M., Wilking, B. A., & Joy,, M. 1984, ApJ, 278, 156

Habing, H.J. 1968, Bull. Astr. Inst. Netherlands, 19, 421

Hasegawa, T., Gatley, I., Garden, R. P., Brand, P. W. J. L., Ohishi, M., Hayashi, M., & Keifu, N. 1989, ApJ, 318, L77

Hollenbach, D. J. & Tielens, A. G. G. M. 1997, ARA&A, 35, 179

Joblin, C., Tielens, A. G. G. M., Geballe, T. R., & Wooden, D. H. 1996, ApJ, 460, L119

Johnson, H. M. 1960, PASP, 72, 10

Lada, E. A., Evans II, N. J., & Falgarone, E. 1997, ApJ, 488, 286

Léger, A. & Puget, J. L. 1984, A&A, 137, L5

Lemaire, J. L., Field, D., Gerin, M., Leach, S., Pineau des Forêts, G., Rostas, F., & Rouan, D. 1996, A&A, 308, 895

Martini, P., Sellgren, K., & Hora, J. L. 1997, ApJ, 484, 296

Martini, P., DePoy, D. L., & Sellgren, K. 1999, *in preparation*

Mathis, J.S. 1990, ARA&A, 28, 37

Nussbaumer, H. & Storey, P. J. 1988, A&A, 193, 327

Oliva, E. & Origlia, L. 1992, A&A, 254, 466

Papoular, R., Conard, J., Guillois, O., Nenner, I., Reynaud, C., Rouzaud, J.-N. 1996, A&A, 315, 222

Puget, J. L. & Léger, A. 1989, ARA&A, 27, 161

Racine, R. 1968, AJ, 73, 233

Rouan, D., Field, D., Lemaire, J.-L., Lai, O., Pineau des Forêts, G., Falgarone, E., & Deltorn, J.-M. 1997, MNRAS, 284, 395

Sellgren, K. 1984, ApJ, 277, 623

Sellgren, K. 1986, ApJ, 305, 399

Sellgren, K., Tokunaga, A. T., & Nakada, Y. 1990, ApJ, 349, 120

Sellgren, K., Werner, M. W., & Dinerstein, H. L. 1983, ApJ, 271, L13

Sellgren, K., Werner, M. W., & Dinerstein, H. L. 1992, ApJ, 400, 238

Sellgren, K. 1994, in The First Symposium on the Infrared Cirrus and Diffuse Interstellar Clouds, eds. R. M. Cutri and W. B. Latter, 243

Sellgren, K., Werner, M. W., & Allamandola, L. J. 1996, ApJS, 102, 369

Spitzer, L. & Zweibel, E. G. 1974, ApJ, 191, L127

Sternberg, A. & Dalgarno, A. 1989 ApJ, 338, 197

Sternberg, A. & Neufeld, D. A. 1999, ApJ, *accepted*

Strom, S. E., Grasdalen, G. L., & Strom, K. M. 1974, ApJ, 191, 111

Strom, K. M., Strom, S. E., Carrasco, L., & Vrba, F. J. 1975, ApJ, 196, 489

Strom, K. M., Strom, S. E., & Vrba, F. J. 1976, AJ, 81, 308

Tanaka, M., Hasegawa, T., Hayashi, S. S., Brand, P. W. J. L., & Gatley, I. 1989, ApJ, 336, 207

Takayanagi, K., Sakimoto, K., & Onda, K. 1987, ApJ, 318, L81

Tielens, A. G. G. M. & Allamandola, L. J. 1987, in Interstellar Processes, ed. D. J. Hollenbach & H. A. Thronson (Dordrecht: Reidel), pg. 397

Turner, J., Kirby-Docken, K., & Dalgarno, A. 1977, ApJS, 35, 281

Uchida, K., Sellgren, K., Werner, M. W., & Houdashelt, M. L. 1999, ApJ, *submitted*

van den Bergh, S. 1966, AJ, 71, 990

Warin, S., Castets, A., Langer, W. D., Wilson, R. W., & Pagani, L. 1996, A&A, 306, 935

Whitcomb, S. E., Gatley, I., Hildebrand, R. H., Keene, J., Sellgren, K., & Werner, M. W. 1981, ApJ, 246, 416

Witt, A. N. & Cottrell, M. J. 1980, ApJ, 235, 899

Wolniewicz, L., Simbotin, I., & Dalgarno, A. 1998, ApJS, 115, 293

Wyrowski, F., Walmsley, C. M., Natta, A., & Tielens, A. G. G. M. 1997, A&A, 324, 1135

This preprint was prepared with the AAS LaTeX macros v4.0.

Table 1. Summary of Observations

UT Date	Source	Offset
1997 Sep 23	NGC 7023 ISO-1	$27''$W $34''$N
1997 Sep 23	NGC 1333 ISO-1	$12''$E $26''$S
1997 Oct 25	NGC 1333 ISO-1	
1997 Oct 26	NGC 7023 ISO-2	$100''$N
1997 Oct 26	NGC 1333 ISO-1	
1997 Oct 27	NGC 1333 ISO-1	
1997 Oct 28	NGC 1333 ISO-1	
1998 Jan 30	NGC 2068 C−Peak	$72''$E
1998 Jan 31	NGC 2023 ISO-1	$60''$S
1998 Feb 01	NGC 2068 H_2−Peak	$121''$E
1998 Feb 02	NGC 2068 C−Peak	

Note. — The slit positions observed for this study. Column 1 shows the date of the observation. Column 2 lists the name of the source, which is a combination of the name of the nebula and a name describing the nebular position. Column 3 lists the offset from the central star of the nebula. This offset position is the center of the $4.5'' \times 45''$ slit oriented North-South. See Section 3 for further details.

Table 2. J and H Band Line Blends

Blend	Line	Wavelength
J1 (1.307 - 1.322 μm)	5-3 S(5)	1.31067
	4-2 S(1)	1.31157
	3-1 Q(1)	1.31410
	9-6 Q(1)	1.31582
	3-1 Q(2)	1.31807
	2-0 Q(9)	1.31877
H1 (1.556 - 1.566 μm)	5-3 O(2)	1.56073
	7-5 S(3)	1.56150
	5-3 Q(7)	1.56263
	4-2 O(4)	1.56352
H2 (1.598 - 1.624 μm)	6-4 Q(1)	1.60153
	6-4 Q(2)	1.60739
	5-3 Q(9)	1.60839
	4-2 Q(13)	1.61225
	5-3 O(3)	1.61354
	6-4 Q(3)	1.61621
	7-5 S(1)	1.62053
	4-2 O(5)	1.62229
H3 (1.666 - 1.678 μm)	6-4 O(2)	1.67502
	5-3 O(4)	1.67182
	6-4 O(2)	1.67502
H4 (1.724 - 1.740 μm)	7-5 Q(1)	1.72878
	8-6 S(2)	1.72967
	6-4 O(3)	1.73264
	7-5 Q(2)	1.73573
	5-3 O(5)	1.73589
	6-4 Q(9)	1.73695

Note. — The prominent H_2 line blends in the $J-$ and $H-$bands in these spectra along with their principal components. Column 1 lists the designation adopted for each blend along with the wavelength range integrated over to measure the blend intensity. Columns 2 and 3 list the transitions and wavelengths of all lines brighter than 1% of 1-0 S(1).

Table 3. NGC 1333 and NGC 2023 Line Intensities

Line ID	Wavelength	$I_{\mathrm{NGC\ 1333}}$	σ_I	$I_{\mathrm{NGC\ 2023\ South}}$	σ_I	$I_{\mathrm{NGC\ 2023\ North}}$	σ_I
3-2 S(2)	2.28703	0.142	0.078			0.080	0.036
2-1 S(1)	2.24772	0.451	0.060	0.401	0.067	0.368	0.043
1-0 S(0)	2.22330	0.703	0.065	0.465	0.062	0.472	0.044
3-2 S(3)	2.20140	0.163	0.057	0.155	0.059	0.162	0.029
2-1 S(2)	2.15423	0.183	0.058	0.155	0.059	0.156	0.033
1-0 S(1)	2.12183	1.000	0.045	1.000	0.043	1.000	0.028
2-1 S(3)	2.07351	0.248	0.046	0.315	0.097	0.293	0.030
1-0 S(2)	2.03376	0.419	0.060	0.422	0.097	0.398	0.067
1-0 S(7)	1.74803	0.122	0.069	0.237	0.083	0.201	0.073
6-4 Q(1)	1.60153	0.130	0.073	0.107	0.064	0.104	0.055
4-2 S(3)	1.26155	0.268	0.135	0.290	0.121	0.244	0.092
J1		0.698	0.218	0.724	0.262		
H1		0.324	0.095	0.212	0.059	0.177	0.071
H2		0.675	0.214	0.480	0.152	0.580	0.215
H3		0.263	0.082				
H4		0.509	0.116	0.390	0.106	0.303	0.119

Note. — Measured line intensities for NGC 1333 and NGC 2023 relative to the 1-0 S(1) line. Column 1 lists the identification for each line, while column 2 lists the central wavelength of the feature. Columns 3 & 4 contain the intensity and 1σ uncertainty for NGC 1333. Columns 5, 6, 7, & 8 contain the corresponding information for the south and north regions of NGC 2023, respectively. These intensity measurements have not been corrected for extinction by dust. The 1σ uncertainties for the 1-0 S(7), 6-4 Q(1), and 4-3 S(3) lines and all of the line blends also contain an additional 5% error to account for the uncertainty in the scaling from J and H to the $K-$band.

Table 4. NGC 2068 Line Intensities

Line ID	Wavelength	$I_{\mathrm{NGC\ 2068-C}}$	σ_I	$I_{\mathrm{NGC\ 2068-H_2}}$	σ_I
2-1 S(1)	2.24772	0.496	0.195	0.376	0.066
1-0 S(0)	2.22330	0.806	0.202	0.488	0.067
2-1 S(2)	2.15423	0.374	0.180	0.183	0.051
1-0 S(1)	2.12183	1.000	0.149	1.000	0.052
2-1 S(3)	2.07351	0.311	0.151	0.275	0.093
1-0 S(2)	2.03376	0.554	0.231	0.466	0.095
1-0 S(7)	1.74803			0.182	0.080
6-4 Q(1)	1.60153			0.132	0.072
J1				0.363	0.143
H1				0.219	0.064
H2		0.761	0.370	0.711	0.195
H3		0.239	0.114		
H4		0.797	0.247	0.396	0.950

Note. — As in Table 3, but for NGC 2068.

Table 5. NGC 7023 Line Intensities

Line ID	Wavelength	$I_{\mathrm{NGC\ 7023\ Peak}}$	σ_I	$I_{\mathrm{NGC\ 7023\ North}}$	σ_I
2-1 S(1)	2.24772	0.290	0.091	0.380	0.161
1-0 S(0)	2.22330	0.411	0.088	0.516	0.164
3-2 S(3)	2.20140	0.150	0.049		
2-1 S(2)	2.15423	0.138	0.061		
1-0 S(1)	2.12183	1.000	0.060	1.000	0.087
2-1 S(3)	2.07351	0.182	0.038	0.241	0.111
1-0 S(2)	2.03376	0.335	0.052	0.411	0.150
1-0 S(7)	1.74803	0.213	0.057	0.471	0.126
H1		0.140	0.067	0.372	0.132
H2		0.347	0.067	0.958	0.364
H4		0.209	0.100	0.637	0.301

Note. — As in Table 3, but for NGC 7023.

Table 6. PDR Diagnostics

Nebula	$\frac{1-0S(1)}{2-1S(1)}$	$\frac{2-1S(1)}{6-4Q(1)}$	$\frac{H4}{1-0S(7)}$	T_{rot}	T_{vib}	γ
NGC 1333	2.26	3.02	4.20	690	5000	1.4
	± 0.32	1.57	2.38	120	720	0.4
NGC 2023 North	2.53	3.37	1.65	920	4540	1.8
	± 0.44	1.93	0.69	250	800	0.7
NGC 2023 South	2.76	3.16	1.52	870	4240	1.9
	± 0.34	1.57	0.76	170	520	0.5
NGC 2068 C-Peak	2.11					
	± 0.91					
NGC 2068 H_2−Peak	2.78	2.07	2.20	1000	4220	1.7
	± 0.53	0.94	0.92	240	800	0.6
NGC 7023 H_2−Peak	3.53		0.98	860	3570	2.2
	± 1.15		0.49	230	1170	0.8
NGC 7023 North	2.70		1.36			
	± 1.19		0.67			

Note. — Line ratios, temperatures, and ortho-to-para ratios for the nebulae discussed in this paper. Column 1 lists the nebula (including the offset position), while columns 2, 3 & 4 list the line ratios of the 1-0 S(1) to 2-1 S(1) lines, 2-1 S(1) to 6-4 Q(1) lines, and H4 blend to 1-0 S(7) line, respectively. The rotation temperature for $v = 1, J = 2, 4$ and the vibration temperature for $v = 1, 2, J = 3$ are listed in columns 5 & 6 in units of Kelvin, while column 7 contains the ratio of ortho− to para−H_2 based on the relative column densities in the $v = 1, J = 2 - 4$ levels. The 1σ uncertainties in all of these quantities are tabulated immediately below them. All of the values listed in this Table have been corrected for interstellar reddening as described in section 4.

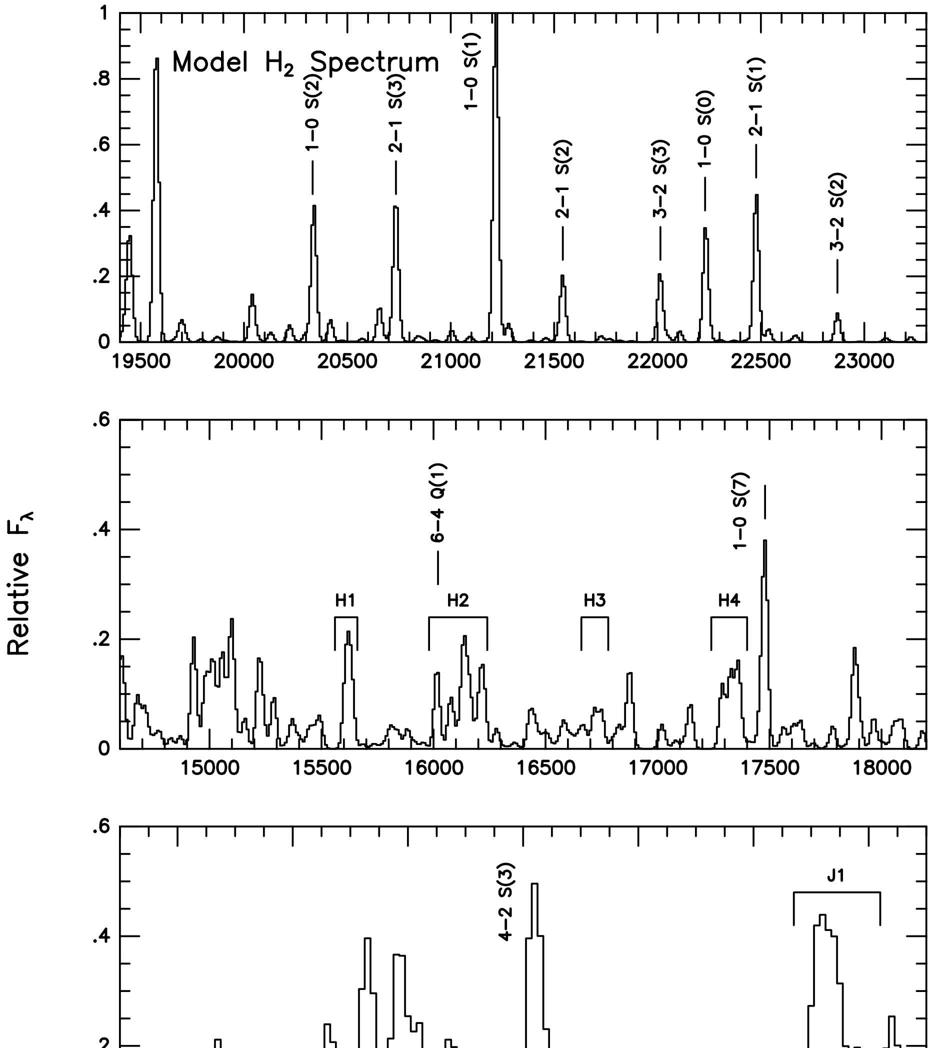

Fig. 1.— A model spectrum of H_2 emission (Draine & Bertoldi 1996) for a density of 10^5 cm^{-3} and incident *UV* field 10^4 times the ambient interstellar field that has been smoothed to our instrumental resolution. We show the near-infrared $J-$, $H-$, and $K-$bands over the same spectral range as our data and have marked the prominent lines and blends detected in most of the objects. The labels J1, H1, H2, H3, and H4 correspond to blends of several lines in the $J-$ and $H-$bands that cannot be easily separated at this resolution. The brightest lines that make up these blends are listed in Table 2.

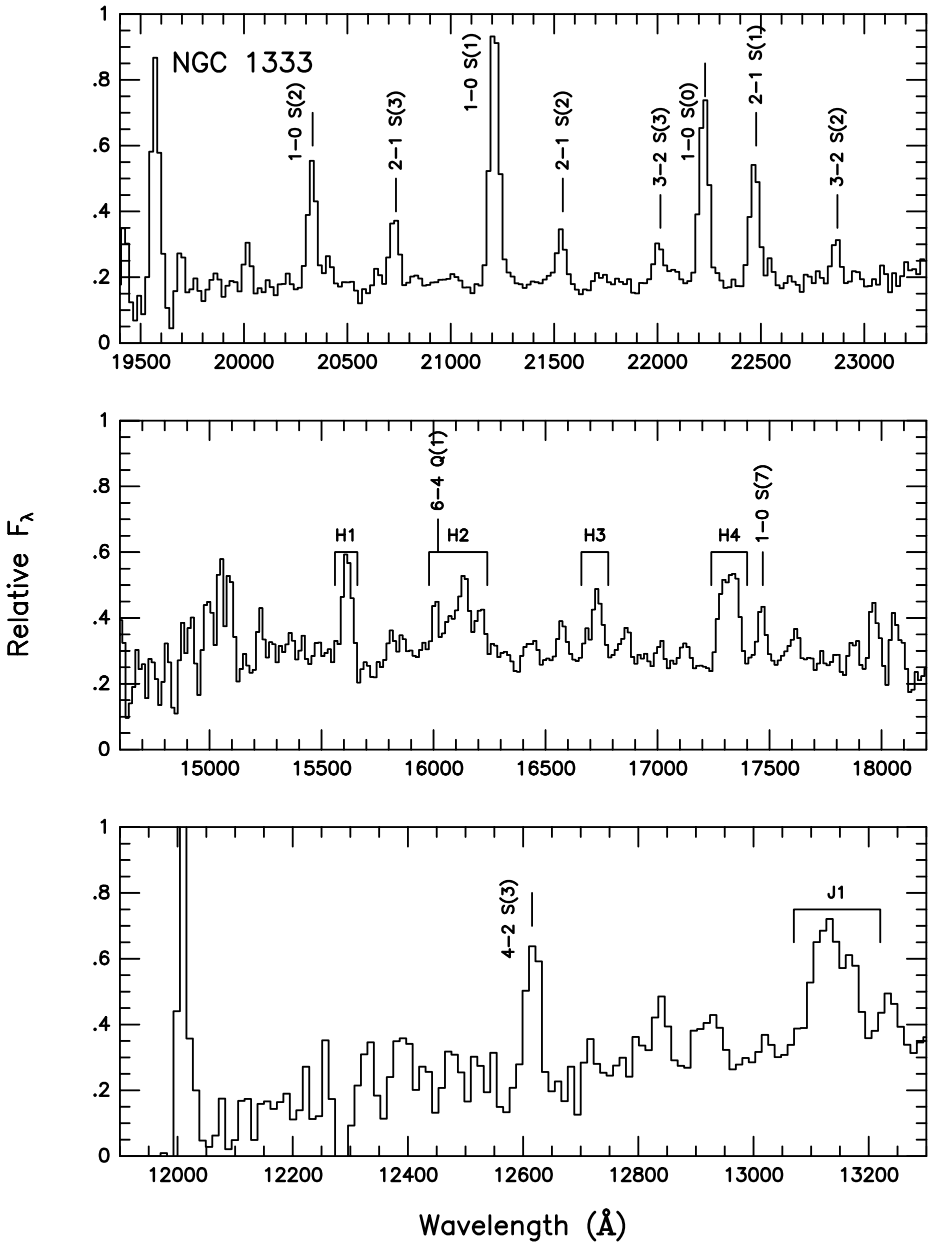

Fig. 2.— Spectrum of NGC 1333 in the near-infrared $J-$, $H-$, and $K-$bands. This spectrum was obtained at a position 12″ east, 26″ south of BD +30 549 and is a summation of all 45″ of the 4.5″−wide, north-south slit (see section 3.1). The spectra are all on the same relative F_λ (flux per unit wavelength) scale as described in section 2.

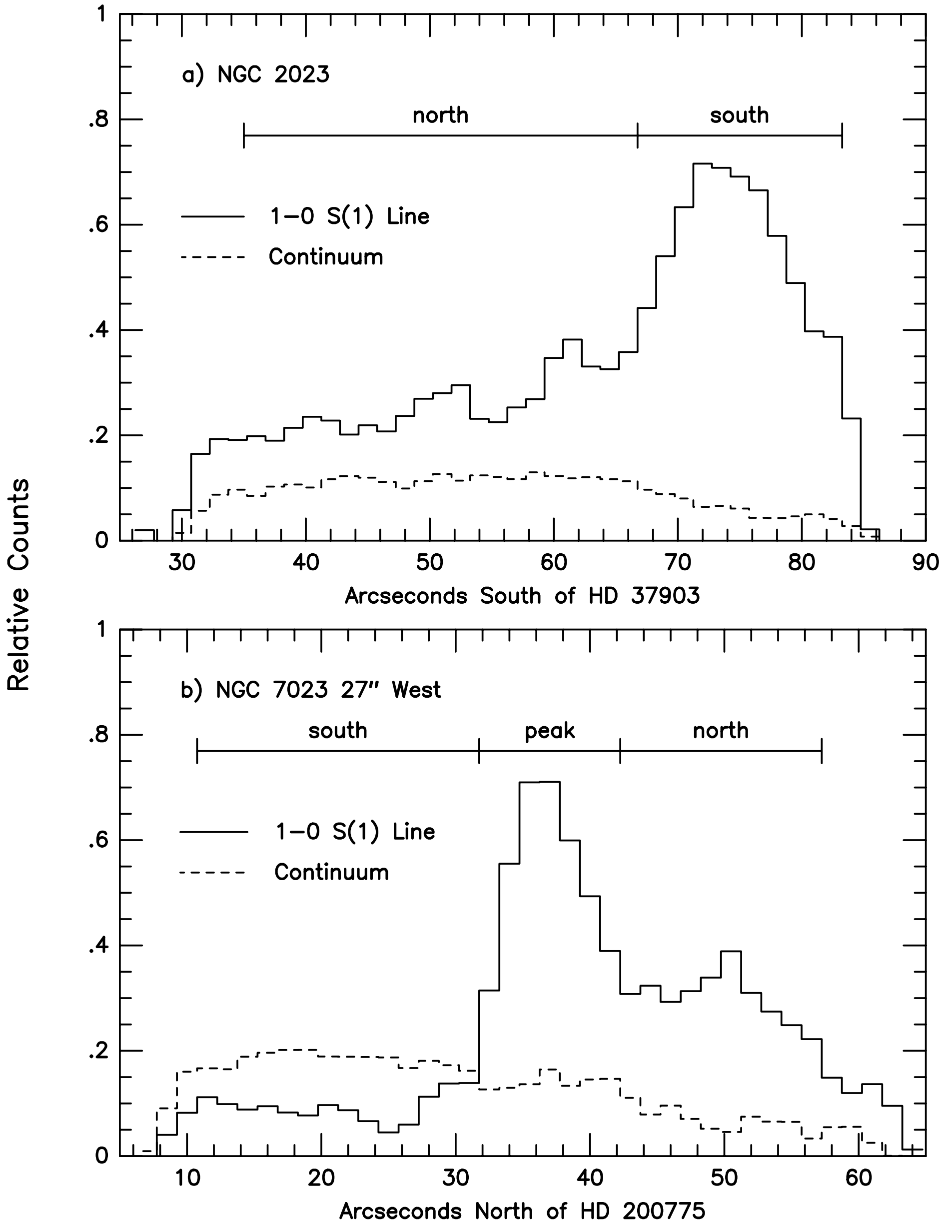

Fig. 3.— Continuum and 1-0 S(1) line intensity along the 4.5″ wide, north-south slit for a) NGC 2023 and b) NGC 7023. The 1-0 S(1) counts were obtained from a 60 Å wide bin centered on the 1-0 S(1) line at 2.121 μm. The continuum counts are the average of two 60 Å wide bins on either side of the 1-0 S(1) emission line. These counts have not been corrected for the slit illumination function. a) The slit was centered 60″ south of HD 37903 with no east-west offset. The two regions marked in the figure are described in more detail in section 3.2. b) For NGC 7023 the slit was centered 27″ west, 34″ north of HD 200775 and the three regions are described in more detail in section 3.4.

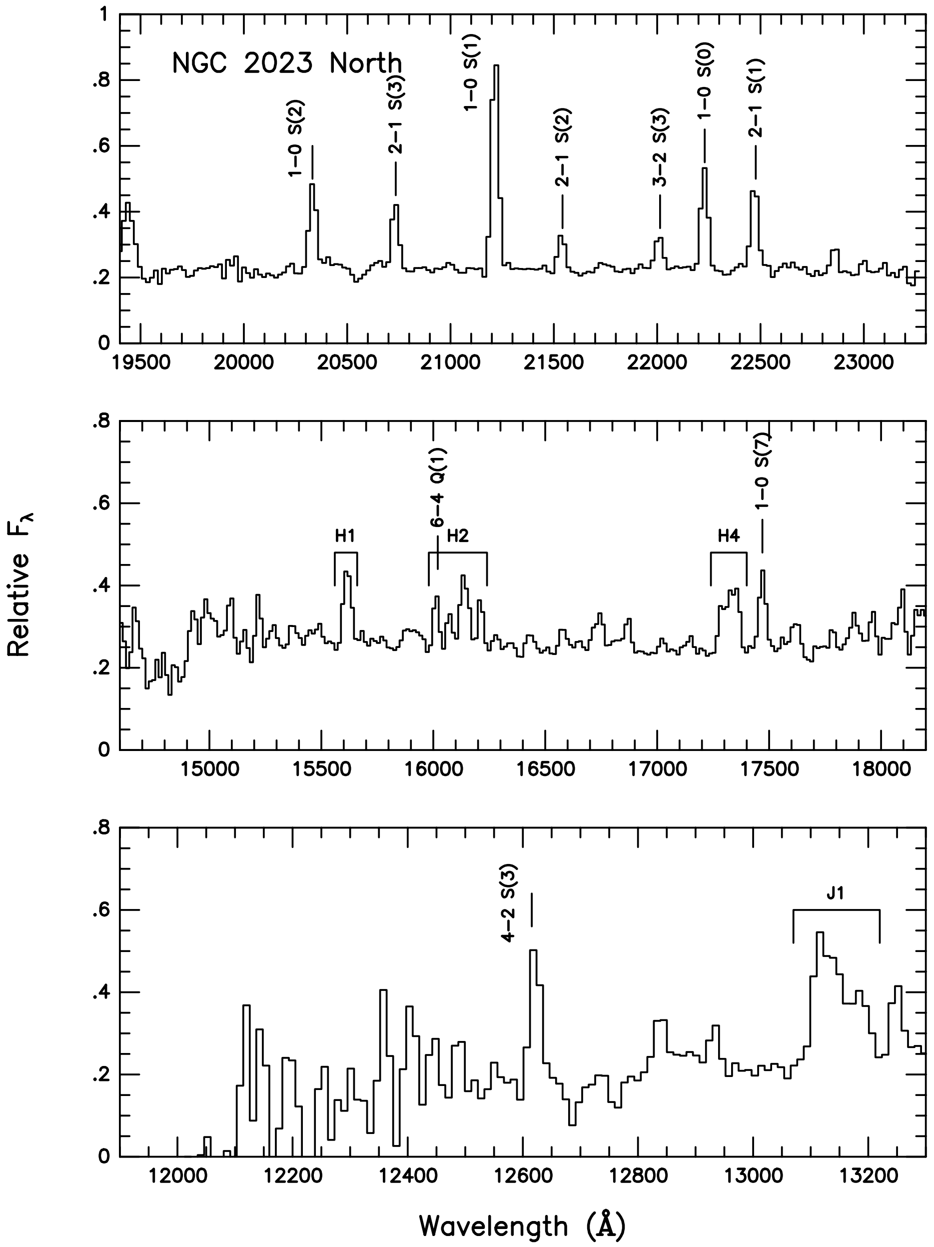

Fig. 4.— As in Figure 2 for the 'north region' of NGC 2023 (see section 3.2). This region extends over $35'' - 67''$ south, $0''$ east of HD 37903 and is bright in continuum emission (see also Figure 3).

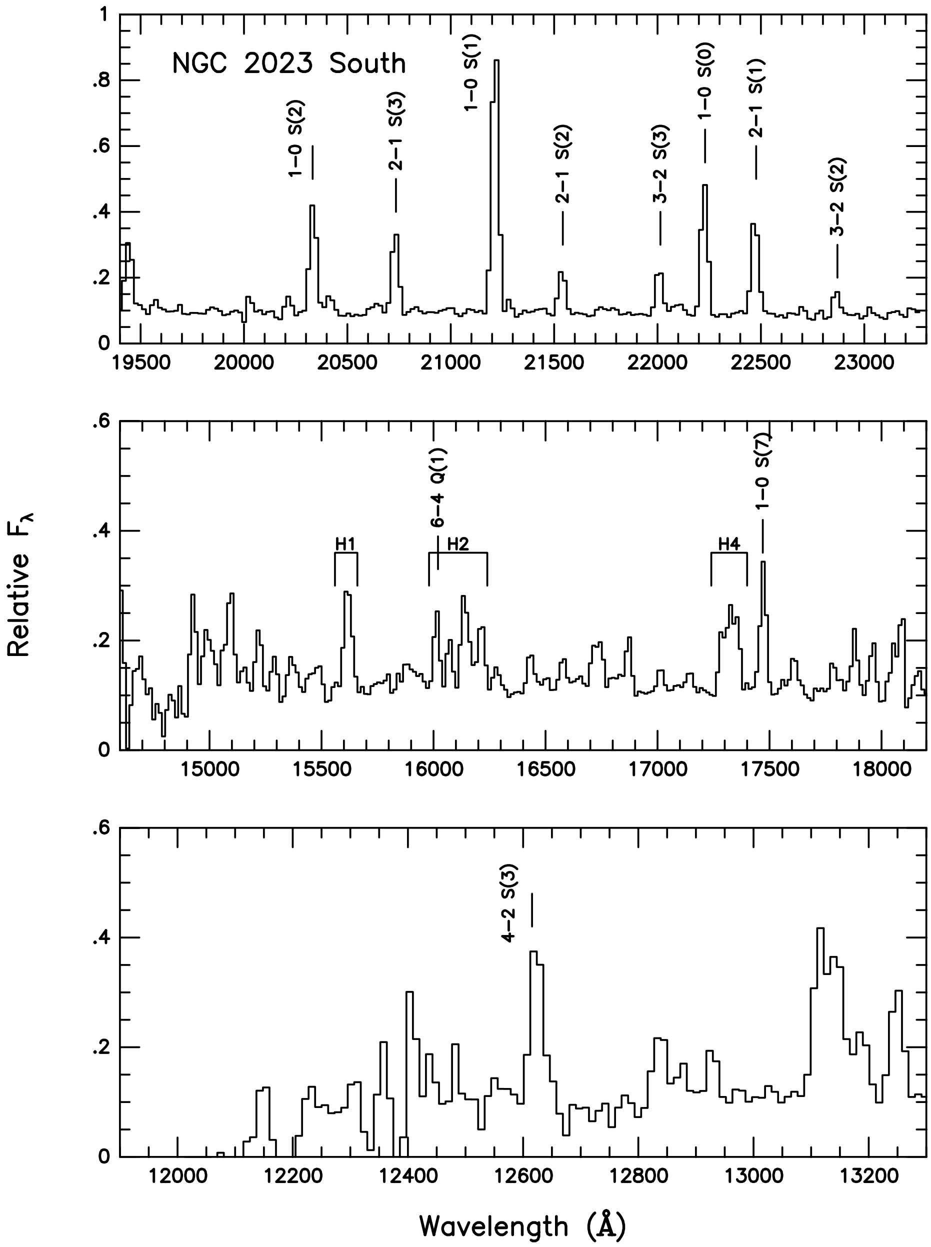

Fig. 5.— As in Figure 2 for the 'south region' of NGC 2023 (see section 3.2). This region extends over $68'' - 84''$ south, $0''$ east and exhibits stronger H_2 emission than the north region shown in Figure 4, but weaker continuum emission (see also Figure 3).

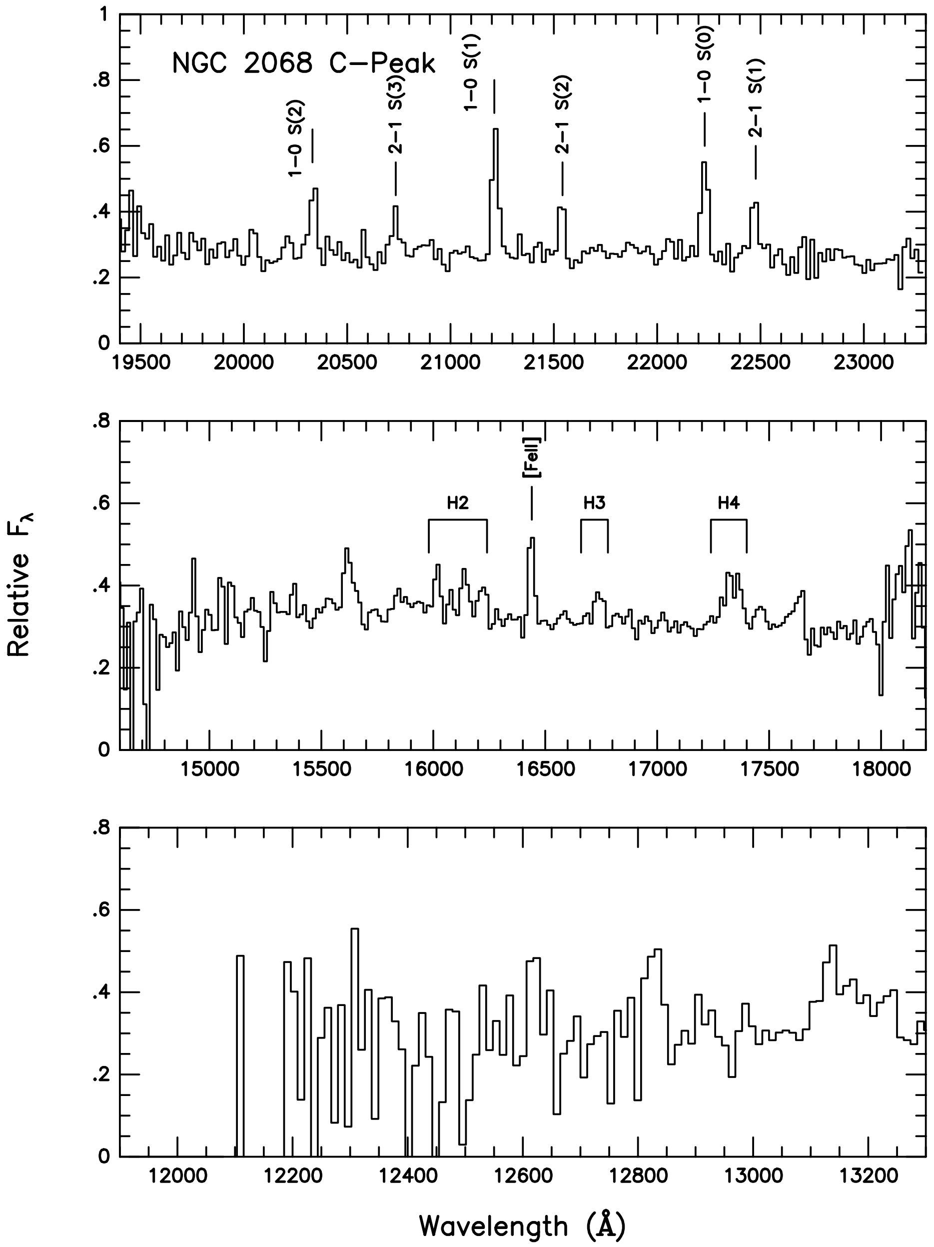

Fig. 6.— As in Figure 2 for the continuum peak in NGC 2068, which is centered 72″ due east of HD 38563-N (see section 3.3). This spectrum is the summation of the entire 45″ of the slit.

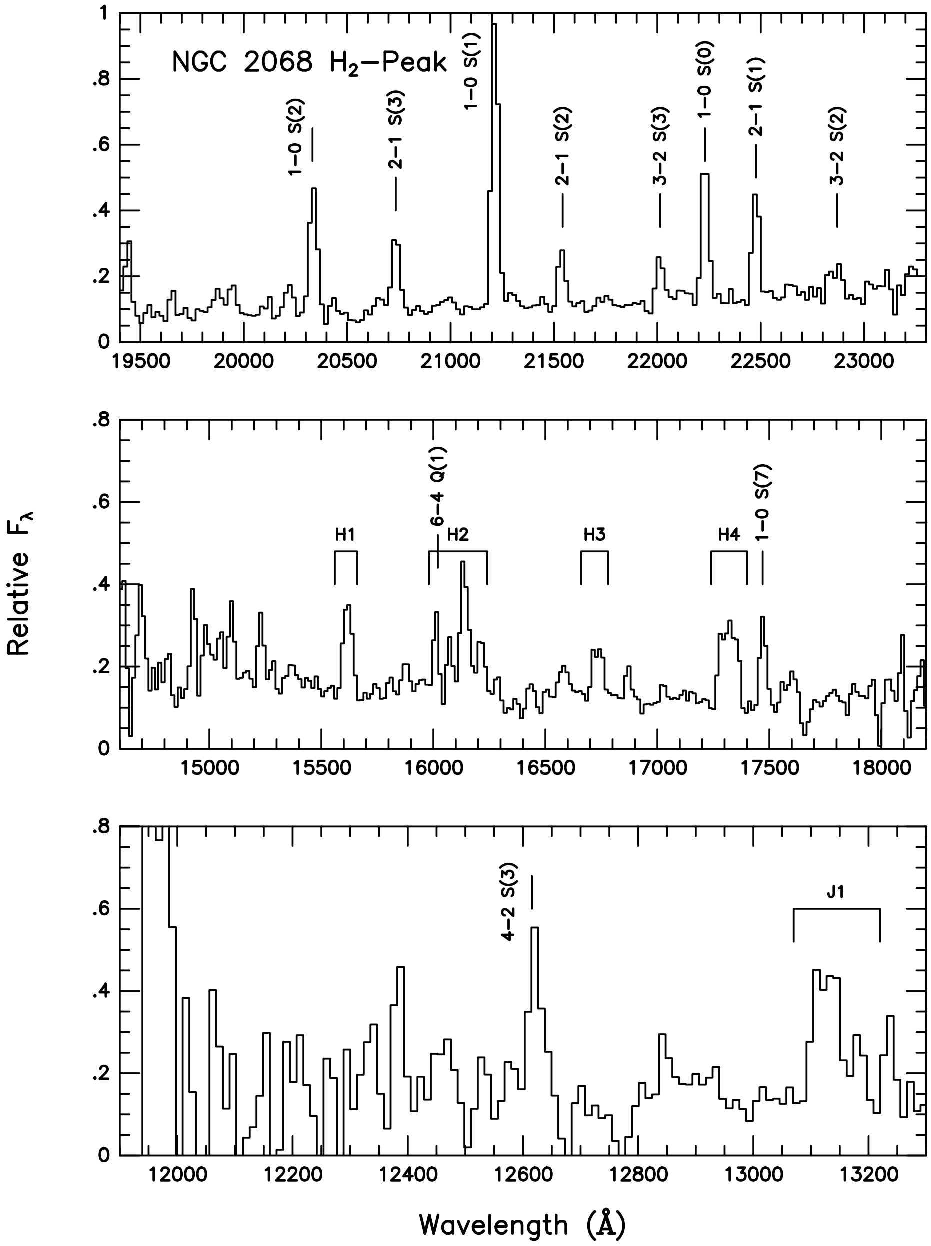

Fig. 7.— As in Figure 2 for the H_2−Peak in NGC 2068, which is centered 121″ due east of HD 38563-N (see section 3.3). This spectrum is the sum of the slit over 0″ − 23″ north of the central double star.

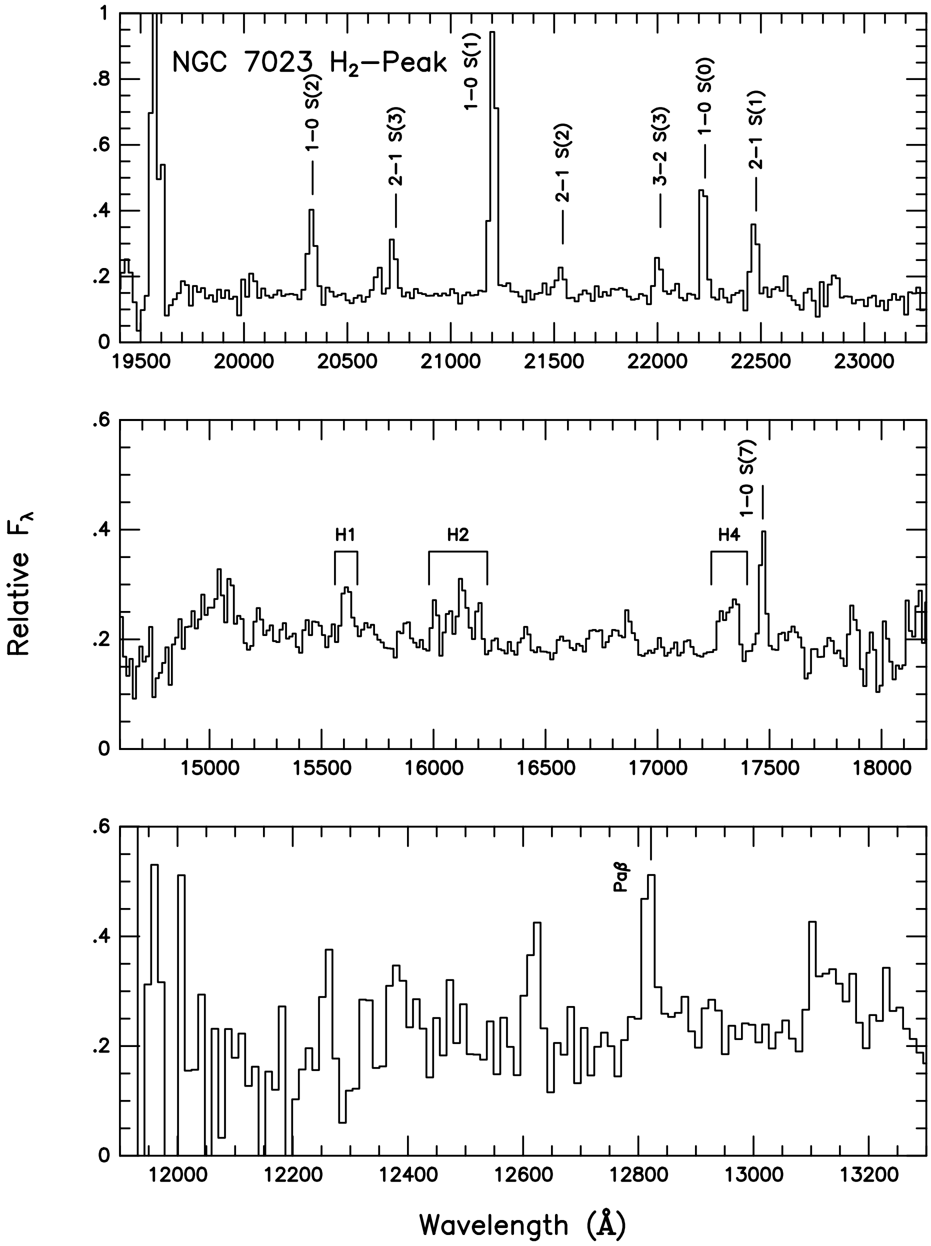

Fig. 8.— As in Figure 2 for the H_2−Peak in NGC 7023 (section 3.4). This region extends over $32'' - 41''$ north at an offset $34''$ west of HD 200775 and contains the strongest H_2 and continuum emission.

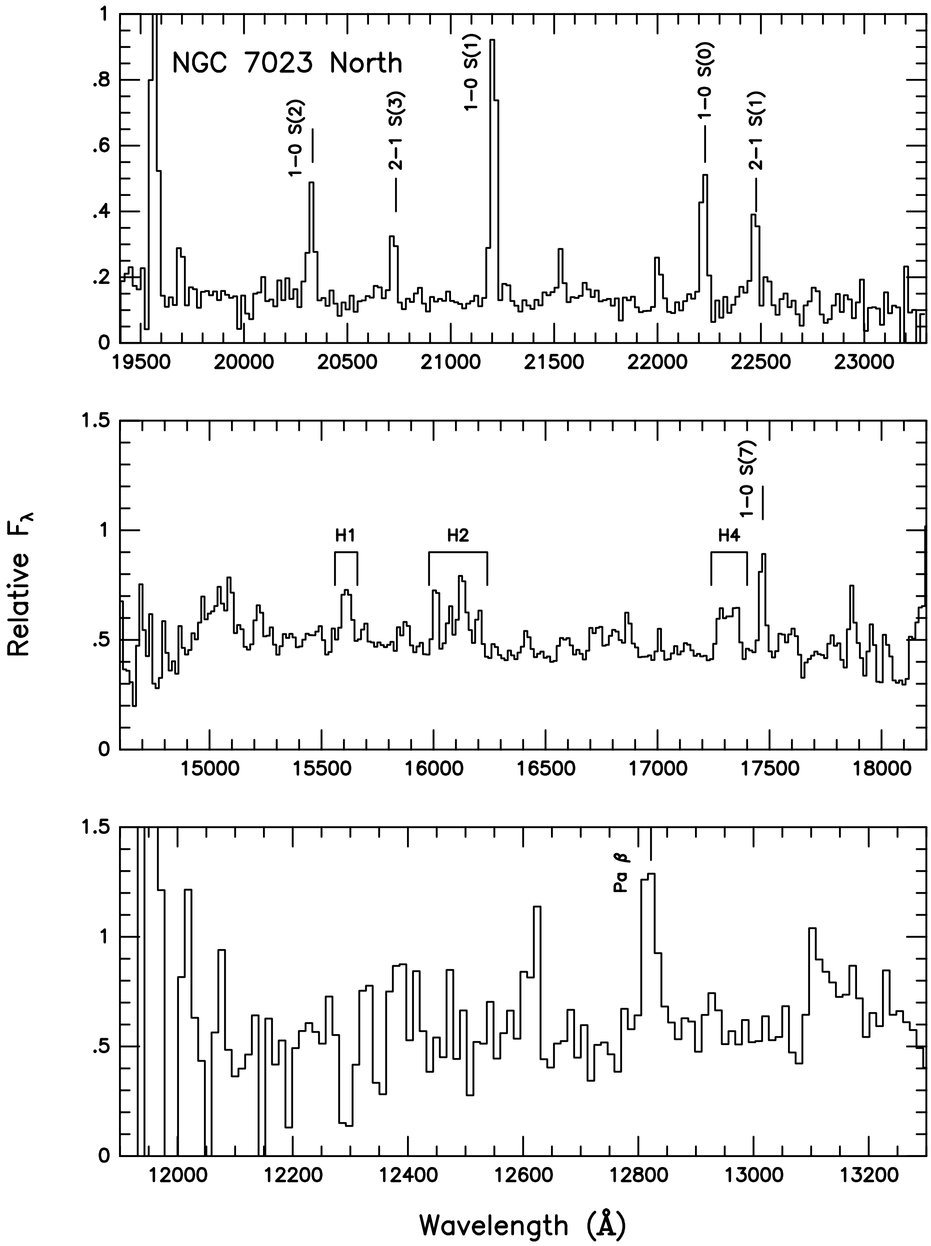

Fig. 9.— As in Figure 2 for the 'north region' in NGC 7023 (see section 3.4). This region extends over 41″ − 56″ north at an offset 34″ west of HD 200775. This region still exhibits bright H_2 emission, but the continuum intensity is significantly less than the H_2−Peak (Figure 8) to the south (see also Figure 2).

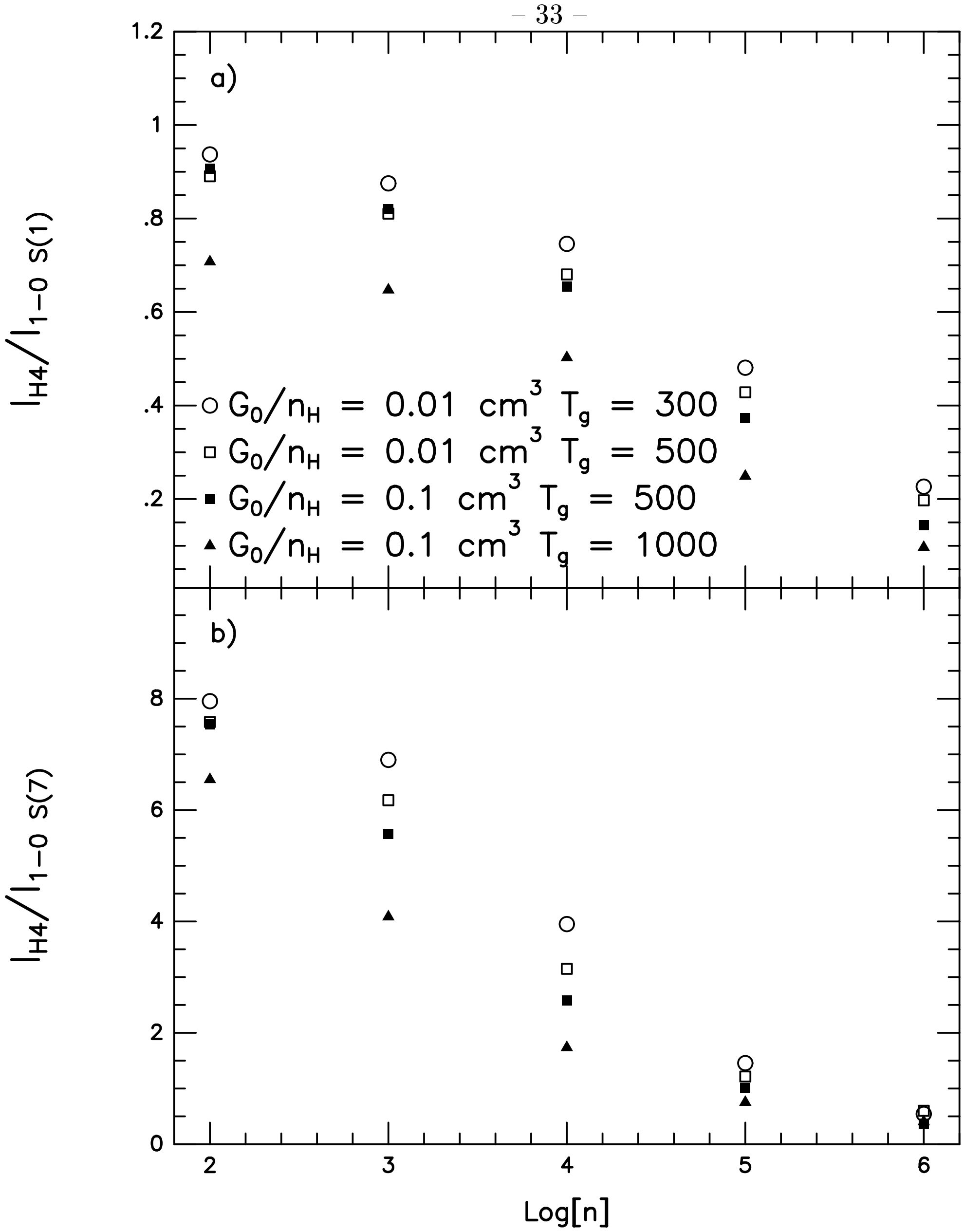

Fig. 10.— a) The way the intensity of the H4 blend (see Table 2), normalized to the 1-0 S(1) line intensity, varies as a function of the PDR parameters in the models of Draine & Bertoldi (1996). The behavior of this blend is representative of the other H_2 blends listed in Table 2 as all of the blends are dominated by transitions from high vibrational levels. b) The ratio of the H4 blend to the 1-0 S(7) line. This pair of features is a relatively good diagnostic of the PDR and has the advantage of being insensitive to the amount of reddening. Our observed values of this ratio vary from 0.98 to 4.20 and fall within the range predicted by the models.

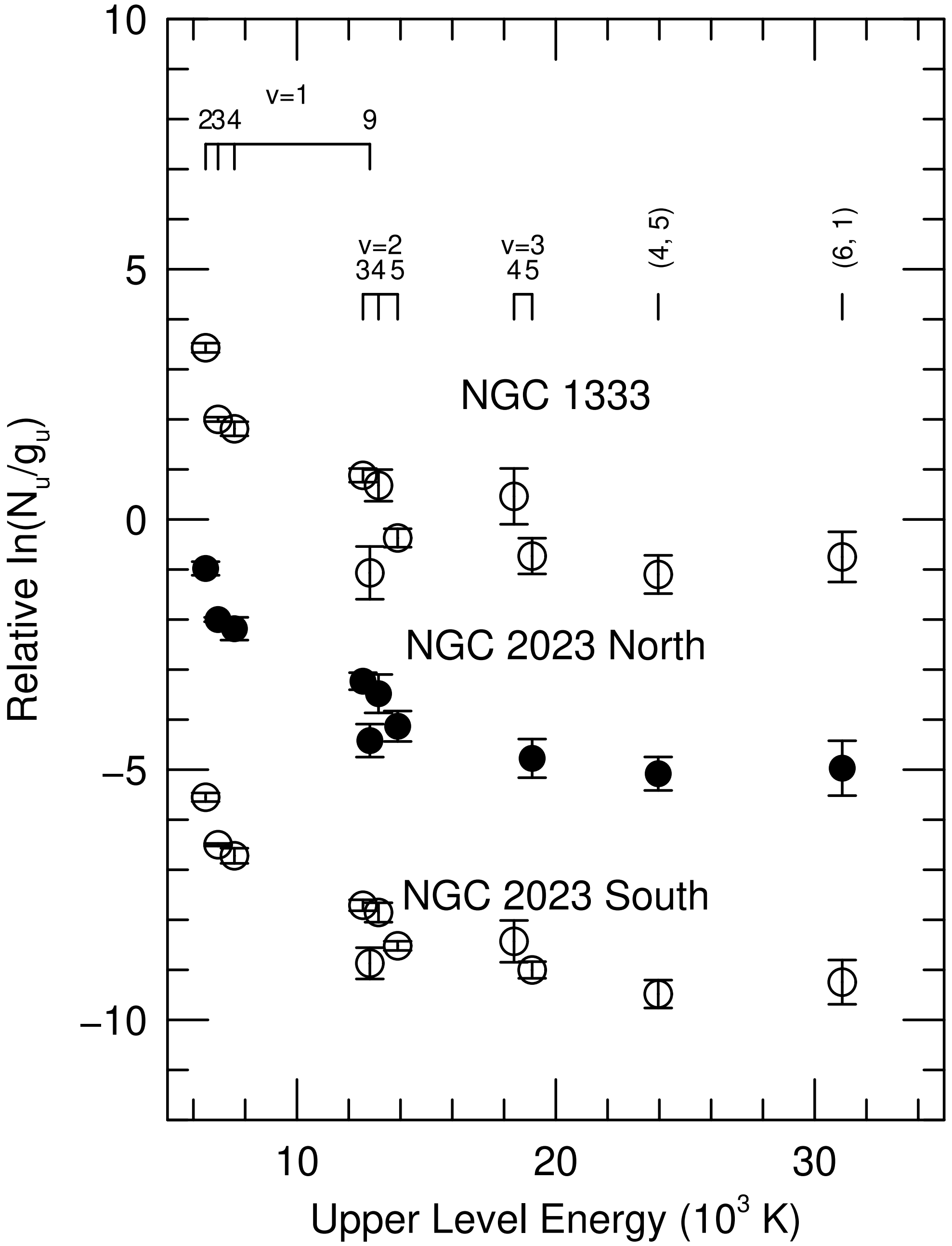

Fig. 11.— Relative Population Diagrams for NGC 1333 and the two slit regions in NGC 2023 plotted as a function of the upper level energy divided by the Boltzman constant. The labels at the top of the Figure provide the rotational (J) and vibrational (v) quantum number of the level giving rise to the observed transition. The quantum numbers in parenthesis, e.g. (4,5), are (v, J). N_u is the column density of the upper level, while g_u is its statistical weight (see section 4).

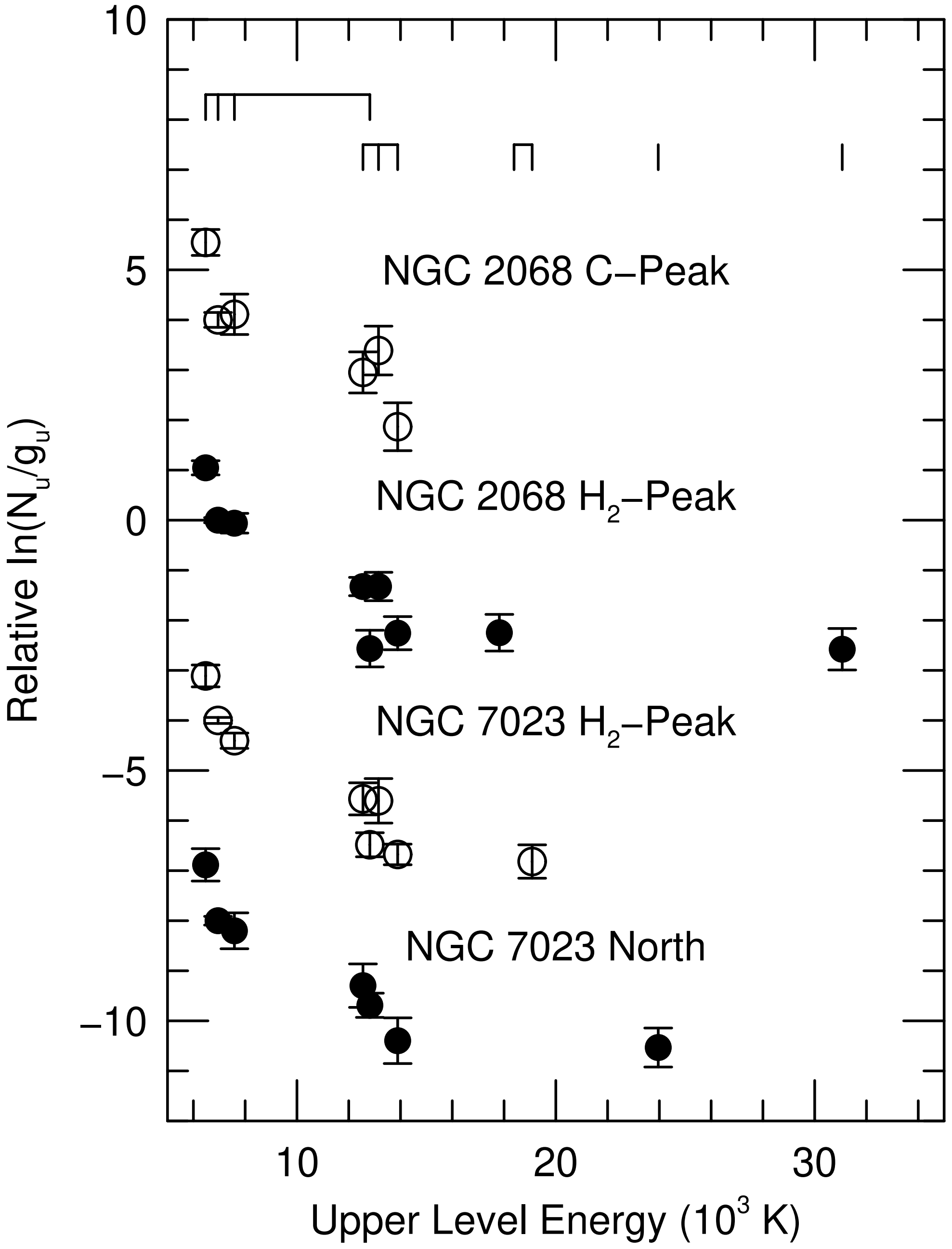

Fig. 12.— Same as Figure 11 but for the continuum and H_2−Peak in NGC 2068 and the H_2−Peak and north region in NGC 7023.